

BUOYANCY EFFECTS AT HIGH ROTATION NUMBER ON THE FLOW FIELD INSIDE A TRIANGULAR SHAPED RIB ROUGHENED CHANNEL

L. Furlani – A. Armellini – L. Casarsa

Dep. of Electric, Management and Mechanical Engineering – University of Udine – Udine – Italy
email: furlani.luca@spes.uniud.it, alessandro.armellini@uniud.it, luca.casarsa@uniud.it

ABSTRACT

The flow field inside a triangular cooling channel for the leading edge of a gas turbine blade has been investigated. The efforts were focused on the interaction between effects of rotation and those induced by turbulence promoters, i.e. perpendicular square ribs placed on both leading and trailing sides of the duct. PIV and Stereo-PIV measurements have been conducted for $Re_{Dh}=10^4$, rotation number of 0, 0.2, and 0.6, and buoyancy parameter equal to 0, 0.08, and 0.7. Coriolis secondary flows are detected in the duct cross section, but contrary to the smooth case, they are characterized by a single main vortex and are less affected by an increase of the rotation parameter. Moreover, their main topology is only marginally affected by the buoyancy forces. Conversely, the features of the recirculation structure downstream the ribs turned out to be more sensible to a change of the sense of rotation and to buoyancy forces.

NOMENCLATURE

D_h	hydraulic diameter	TS	trailing side
Bo	buoyancy parameter	u,v,v',w	velocity fluctuations on x, y, y', z directions
LS	leading side		
R_x	radius of rotation	U_b	bulk flow velocity
Re_{Dh}	Reynolds number	U,V,V',W	mean velocity components on x, y, y', z directions
Ro	rotation parameter		
T_b	bulk flow temperature	x,y,z	radial, peripheral and normal coordinates
T_w	wall temperature		
Tu	Turbulence intensity computed on u,v,w	y'	wall normal direction
$Tu_{xy'}$	Turbulence intensity computed on u,v'	Ω	rotational speed

INTRODUCTION

The study about the effects introduced by rotation on the thermal and flow fields inside cooling channels used for rotor blades of gas turbines has seen in the last years a growing interest in the research community. When a specific cooling passage is subjected to rotation, two are the main physical phenomena that can have an impact on the coolant path: the rise of Coriolis forces and the appearance of buoyancy effects (Johnston et al., 1972, Morris and Ayhan, 1979). The former effect is usually characterized by the rotation parameter ($Ro=\Omega D_h/U_b$) which takes into account the relative importance between peripheral velocity and bulk flow velocity. More precisely, the Coriolis acceleration ($a_c=-2\Omega \times \mathbf{C}$, where \mathbf{C} is the relative velocity vector) that acts on the relative flow inside the duct causes the establishment of a spanwise pressure gradient that counterbalances its effects. If a confined flow with non uniform velocity distribution is considered, a local unbalance between pressure gradient and Coriolis forces is found inside the region of low momentum fluid, hence a local flow deflection is induced and a secondary vortical flow establishes in the duct cross section, as sketched in Fig. 1. In the rather common case of a radial outward flow inside a rectangular channel, the slower near wall flow is pushed towards the leading side (LS) of the duct by the

Coriolis induced pressure gradient, consequently a symmetrical pair of vortex cells rises which displace the core fluid towards the trailing side (TS) of the duct (Speziale and Thangam (1983)).

The second main effect of rotation is described by the buoyancy parameter ($Bo = Ro^2 R_x / D_h (T_w - T_b) / T_b$), which expresses the ratio between buoyancy forces and bulk flow inertial forces. The Bo parameter is proportional to Ro^2 and depends on the ratio between the local radial position (R_x) and duct hydraulic diameter (D_h). The effect is triggered by a non uniform fluid temperature, hence density, distribution that can be characterized by the temperature difference existing between the walls (T_w , usually hotter than the fluid) and the bulk flow (T_b). More precisely, the hotter (hence with lower density) near wall fluid experiences a lower centrifugal force than the colder (hence with higher density) core fluid.

The most recent contributions in the open literature that deepen the comprehension about these phenomena for application to gas turbine cooling channels deal with the study of the interaction between rotation effects and adoption of turbulence promoters (Coletti et al., 2012) on the channel walls. Complex geometries have also been investigated, such as triangular (Pascotto et al., 2014), trapezoidal shaped (Armellini et al., 2011, Mucignat et al. 2013) and multipass channels with bends (Elfert et al. (2012) and Lei et al. (2014)). For a simplified channel configuration (single-side rib-roughened rectangular channel with radial outward flow) Coletti et al. (2012) showed that the separating/reattaching flow pattern promoted by the ribs is highly affected by rotation. In particular, if the background flow vorticity has the same orientation of the angular velocity of the rotating system (i.e. what is found on the LS of a rectangular channel with radial outward flow) a stabilizing effect on the boundary layer is induced and a wider recirculation area is found downstream of the obstacles, vice versa on the opposite side. If non isothermal conditions are also considered (Coletti et al., 2014), buoyancy effects cause an higher mixing in the near wall flow, with much higher effects on the stabilized side wall where the extension of the separated flow region is further increased, conversely less significant differences are found about the extension of the recirculating flow on the opposite wall.

In the case of rectangular or square channels in orthogonal rotation (i.e. with the rotation axis parallel to the duct height) the basic description about the rotational effects reported above allows a rather good prediction about the main flow features that rise inside the passage. On the other hand, if more complex geometries are considered, the analysis is rather less trivial as shown by Armellini et al. (2011) and Mucignat et al. (2013) for a trapezoidal channel used for trailing edge cooling or in case of a triangular leading edge passage investigated by Pascotto et al. (2014). In particular, the latter contribution showed that inside a smooth triangular channel a non symmetrical Coriolis vortices pair is found, with separation and reattachment points that are no longer located about the mid span of the lateral walls, but are found on the triangle upper apexes. Moreover, a steady flow configuration is never reached, indeed as the flow develops along the channel more than two Coriolis vortical cells are found inside the channel cross section. The phenomenon is caused by a periodical reversal of the spanwise velocity component (i.e. the velocity component normal to both the rotation axis and the radial direction) inside the low momentum region found at the leading apex. The overall behaviour is strongly fastened if Ro is increased.

The present work is the first part of a research activity that aims at extending the previous findings about the rotational effects inside triangular shaped ducts by considering also the effects of turbulence promoters and by introducing buoyancy effects. In particular, experiments have been

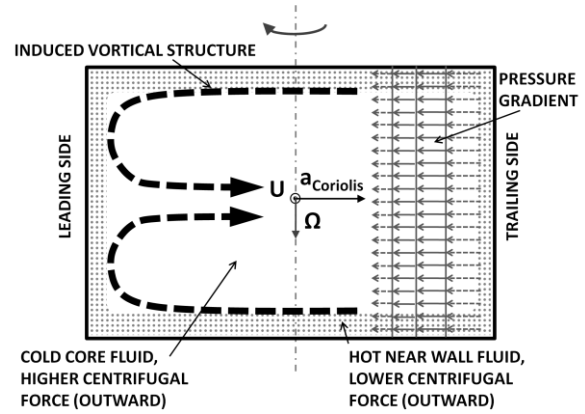


Figure 1: **Illustration of forces and main flows features found in a rotating duct**

conducted on the same rig used by Pascotto et al. (2014) but on a modified test section that allows the heating of the lateral walls that have also been equipped with square orthogonal ribs (see Fig. 1). As in Pascotto et al. (2014), the choice for this simple geometry (i.e. a single passage duct with an equilateral triangle cross section and without extraction holes for film cooling) is motivated by the availability of a wide thermal analysis provided by Liu et al. (2009, 2010), that can be complemented by the present findings.

TEST RIG AND EXPERIMENTAL METHODOLOGY

Test rig

The present experimental activity has been conducted on the facility of the Turbomachinery and Energy System Laboratory of the University of Udine. A detailed description of the rig can be found in Armellini et. al (2011). The facility has been designed to allow detailed flow field investigations inside rotating ducts representative of modern cooling system for gas turbine blades and has been recently upgraded for thermal measurements as well. In particular the system has been provided with a rotary fluidic joint (Fig. 2(a)) equipped with 32 slip rings used for signal and electric power transmission on board of the rotating system.

The test section consists of a straight channel 820 mm long with an equilateral triangle cross section of side $L=130$ mm, (Fig. 2). Square ribs of height $h=6.5$ mm are placed perpendicularly to the channel main axis on the two lateral walls. As done by Liu et al. (2009, 2010), the ribs have a pitch of $8h$ and have a staggered disposition with respect to the two channel sides. In order to investigate buoyancy effects, each ribbed wall has been machined out of a single aluminium slab. Heating is provided by powering with direct current a $25 \mu\text{m}$ thick Inconel sheet attached on the external surface of the wall (Fig. 2(e)). A further layer of insulating material minimizes the thermal losses towards the environment. The temperature of each heated wall is monitored with 4 thermocouples installed inside the aluminium walls (Figs. 2(c,e)) in the inter-rib regions just

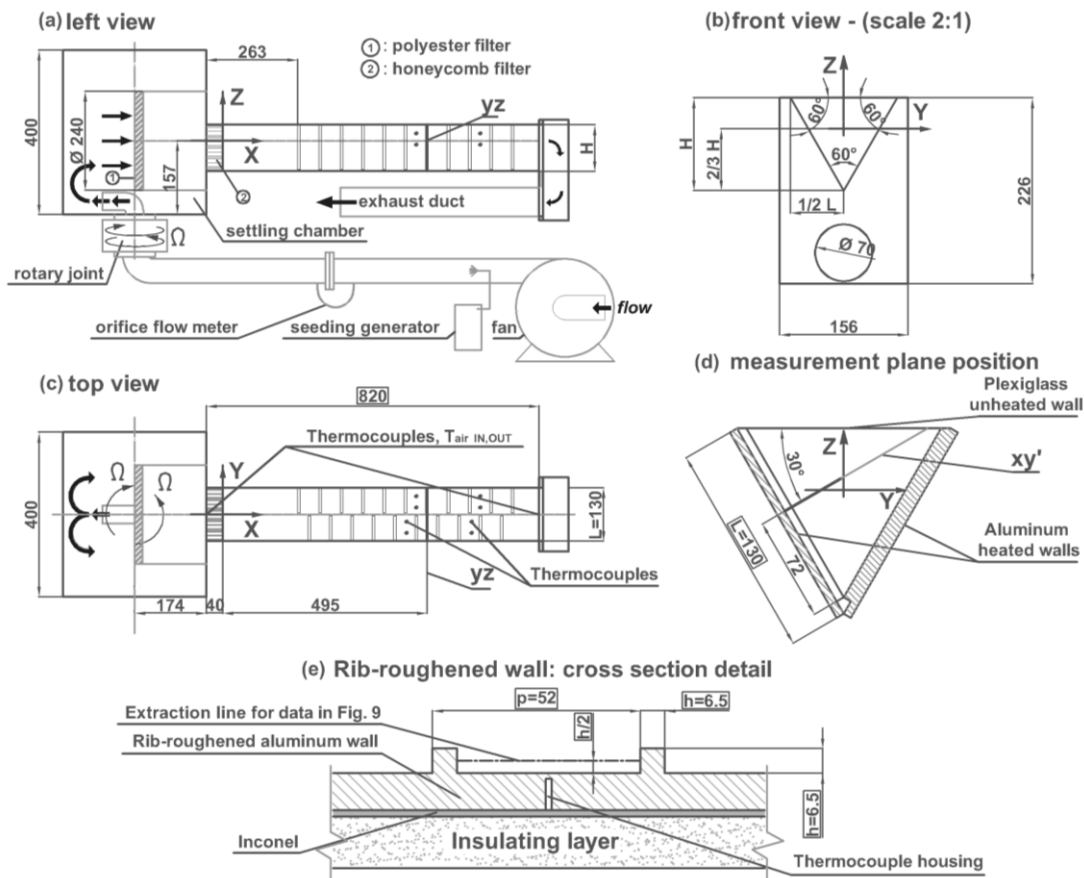


Figure 2: Experimental facility, nomenclature and positions of the PIV measurement planes

upstream and downstream the investigated area (planes yz and xy' in Figs. 2(c,d)). The calibration of the temperature sensor (connected to the slip rings) and a data averaging process computed on stencils of 20 samples acquired at 2 Hz lead to an overall uncertainty of ± 0.75 K. The hot test conditions have been obtained by heating up the ribbed walls up to 110 °C. Differences of 1K have been observed between the readings of two thermocouples placed on similar points of the same wall but in the two different inter-rib locations, while the maximum difference between the hottest and the coldest readings was equal to 5 K and has been observed for tests at the highest rotational speed.

The test section is fed with air at ambient conditions thanks to a rotating settling chamber connected to the rotary fluidic joint. The settling chamber design (Fig. 2(a)) is such that a uniform flow distribution is ensured at the duct inlet, where a 40mm long honeycomb filter prevents also from flow separation. At the channel outlet, the exhausted flow is collected in a small settling chamber and then leaves the test section through a return passage, so avoiding any flow perturbation near the tip region that could conversely occur under rotation if a free radial outlet was set.

Flow field measurement methodology

Flow field measurements were performed by means of 2D and Stereo-PIV techniques. A single camera configuration (Fig. 3(a)) for 2D measurements was used on plane xy' (Fig. 2(d)), while a double camera configuration (Fig. 3(b)) for Stereo-PIV measurements was used on plane yz (Fig. 2(c)). The PIV system is custom-made and was already described in Mucignat et al. (2013).

The PIV raw data (PIV image pairs) were processed using the commercial software PIVview (from PIVTEC GmbH). In particular, for the Stereo-PIV data, image back-projection and then stereo reconstruction were performed; furthermore, a disparity correction was also used in order to minimize the misalignment errors (Willert, 1997). Stereo calibration of the measurement chain was achieved inside the channel, by means of multiple images of a target placed at first on the image plane and then displaced in six adjunctive off-plane positions. The nominal magnification of the PIV images ranges from 17 px/mm (Stereo-PIV) to 20 px/mm (2D-PIV), which turns in a vector resolution from 1.06 to 1.25 vectors/mm, respectively.

As can be seen from Fig. 3, the present PIV system is fixed, i.e. not rotating with the test section. Consequently, the measurements at $Ro > 0$ are carried out in phase-locked mode and, therefore, the direct output of the PIV raw data is the absolute flow field. The relative field inside the test section is obtained by subtracting the local peripheral displacement of the system from the PIV data with an ad-hoc procedure. For the case of PIV measurements conducted on flow planes perpendicular to the rotation axis, Armellini et. al (2012) proposed a specific pre-processing methodology to be applied on the PIV raw data (image pairs) and that allows to keep the peripheral displacement subtraction error below 1%, i.e. allows to provide a final accuracy level close to the one of standard 2D measurements on static test sections. Unfortunately, the aforementioned methodology cannot be directly used for the present case because the selected measurement planes are not perpendicular to the rotation axis. Indeed, because a component of the peripheral displacement lies on the out-of-plane direction, a correct image reconstruction would need a precise knowledge of the perspective view realized by the optical system, resulting in a rather complex

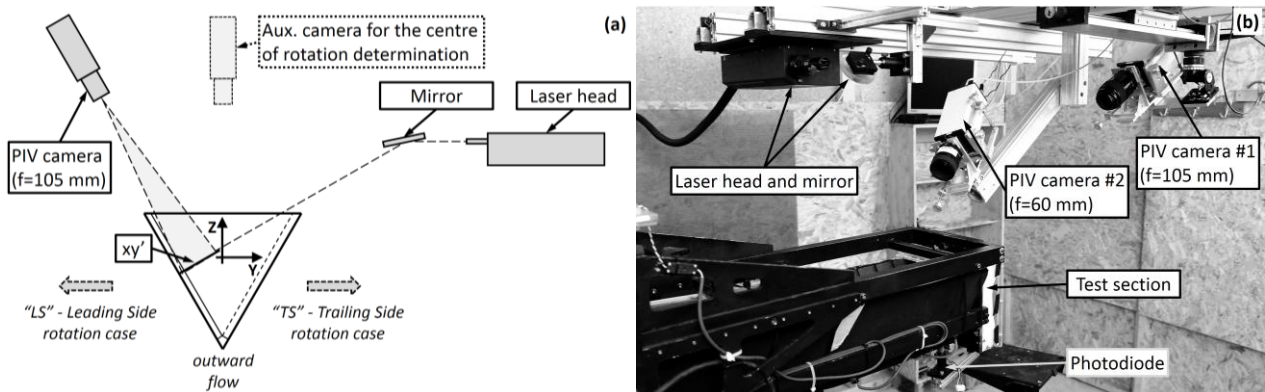


Figure 3: Measurement set-up used for 2D-PIV on plane xy' (a) and Stereo-PIV on plane yz (b)

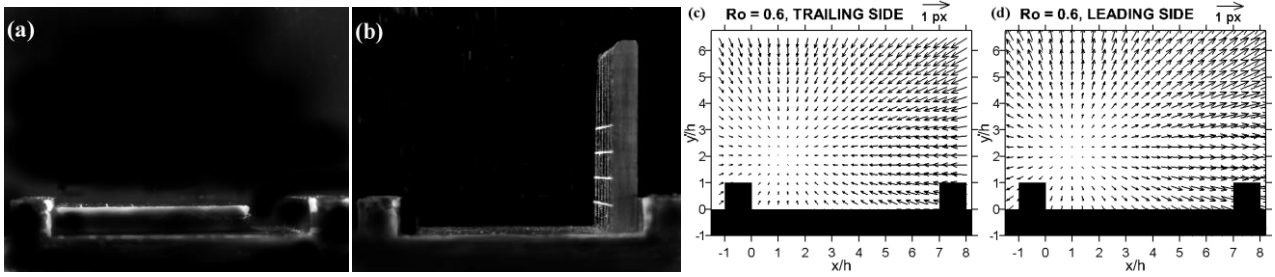


Figure 4: **Parallax error compensation for 2D xy' measurements: examples of target images (a, b) and of displacement correction fields (c, d)**

implementation of the methodology. In view of this, a different approach has been chosen, namely the second exposure of each PIV image pair has been pre-processed by applying a rigid translation of the image in order to reduce the walls' displacement at less than 1 px with respect to the first exposure. This raw peripheral displacement subtraction allows the PIV image processing algorithm to resolve particle displacements of standard magnitude (± 10 px) and to impose the correct boundary conditions on the processing mesh (i.e. no-slip condition at the solid walls). Successively, the displacement components applied for the rigid image translation are added to the resulting data in order to restore the absolute velocity field. The post-processing procedure is then completed by the subtraction of the real peripheral velocity field, which is accurately measured as described at the end of this section.

The processing of the 2D data is further complicated by the need to compensate for the parallax error associated to the out-of-plane component of the peripheral displacement (plane xy' is not perpendicular to the rotation axis). More in detail, even if rather long focal lenses have been used, it is not possible to assume that the light is collected with parallel rays; consequently, the out-of-plane particles displacement results in a wrong in-plane component which magnitude is proportional to the distance between a specific measurement point and the intersection of the camera optical axis with the measurement plane. For the present data on plane xy' , the maximum magnitude of the out-of-plane peripheral displacement was 14 px, hence the resulting in-plane parallax component can be up to 0.9 px, that is a not negligible value. A precise parallax error compensation requires the knowledge of two main input data: the lenses focal length and the position of the optical axis projection on the image plane. For sake of accuracy, the actual value of the lens focal length has been directly measured with a dedicated procedure (i.e. to measure the size of the field of view framed with the present optical configuration) and resulted to be equal to 108.5 mm. Optical axis projection position has been determined by an in-situ calibration realized with a target that allows to frame straight lines aligned with the out-of-plane direction on planes either parallel (Fig. 4(a)) or perpendicular (Fig. 4(b)) to the channel wall. An iterative procedure is carried out in order to find the position where an out-of-plane line is viewed as single point, namely the projection of the camera optical axis on the image plane. Examples of parallax error compensation displacement fields are reported in Figs. 4(c, d) for the case $Ro=0.6$. As can be seen, the projection of the lenses optical axis has been placed close to the area where flow recirculation is supposed to be found, this choice guarantees that the most critical area of the analysed flow field is only marginally affected by the parallax error and by the possible uncertainties of its compensation.

The determination of the peripheral displacement field requires to know the real position of the measurement points with respect to the rotation axis, the test section angular velocity, and to ensure a reliable synchronization of the PIV system with the test section angular position. Concerning the centre of rotation position evaluation, a two steps indirect methodology has been used. As a first step, the procedure proposed in Armellini et al. (2012) is followed, namely a target with a rectangular grid of dots is placed inside the test section on plane $z=0$ and it is framed by an auxiliary camera with optical axis parallel to the axis of rotation (aux camera in Fig. 3(a)). Two exposures of the target are taken with the test section at two angular positions. Markers centre positions are determined in the two images by means of a cross-correlation with a sample signal. Afterwards, the

centre of rotation position can be determined applying a least square method on the markers displacement. Using a large number of dots it is possible to provide the definition of the centre of rotation with an accuracy of ± 0.1 mm with respect to a reference point of the target. The second step requires to operate the laser and to acquire an image of the laser sheet trace on the calibrated target. The analysis of this realization allows to get an accurate determination of the position of the laser sheet trace with respect to the centre of rotation. The last technical issues that have to be addressed are the synchronization of the PIV system with the test section rotation and the measurement of the actual peripheral velocity. Both these issues are solved by sampling the TTL signal from a photodiode (see Fig. 3(b)) periodically screened by the test section, all the technical details can be found in Armellini et al. (2011). The mean angular velocity for each revolution, Ω , can be computed with a relative error equal to $\delta\Omega/\Omega=3.5 \times 10^{-7}$, while image positioning stability is kept by far smaller than the data spatial resolution (i.e. with image shifts about ± 1 pixel), so reducing to negligible values the spatial averaging error.

Uncertainty analysis

Concerning PIV data accuracy, only statistical flow quantities will be presented, resulting from the ensemble average of 10^3 instantaneous samples. For a static 2D measurement, the overall upper bound estimate of the mean velocities uncertainty results to be less than 2% with respect to U_b (95% confidence level), while the maximum uncertainty in the estimate of the higher order statistics is 5% of U_b . For the data acquired under rotation, the pre- and post-

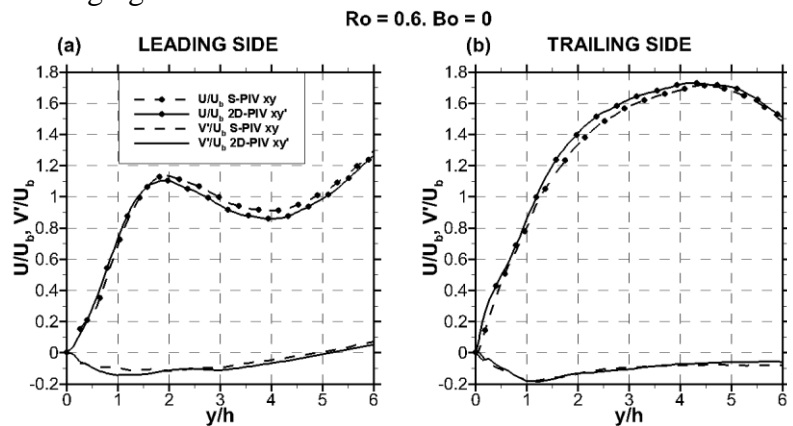


Figure 5: Comparison of 2D and Stereo-PIV data extracted on the intersection line of xy' and yz planes of U and V' profiles from 2D-PIV on xy' and S-PIV on yz

processing procedures used for the peripheral displacement field subtraction introduce further unavoidable error sources that increase the overall uncertainty on the mean velocities up to 5% of U_b . A proof of the reliability of this estimation is provided by Fig. 5, where a cross comparison between 2D and Stereo-PIV data is provided for the most critical case of $Ro=0.6$. The plots clearly show a rather good superimposition of the data with maximum differences of about $0.05U_b$.

Test conditions

All tests have been conducted at $Re_{Dh}=10^4$ defined on the duct hydraulic diameter ($D_h=75.05$ mm) and on the air bulk velocity ($U_b=2.1$ m/s) and conditions measured at the inlet of the test section (see $T_{air,in}$ in Fig. 1(c)). Rotation numbers of 0.2 and 0.6 have been reached by spinning the test section at about 55 and 160 rpm, respectively. Ribbed walls temperatures of about $110^\circ C$ corresponded to $Bo=0.08$ and 0.7 at the radial position where the measurement plane yz is found ($R_x=709$ mm) and for the two rotating conditions of $Ro=0.2$ and 0.6 , respectively. The present working conditions are considered to be representative of current engine conditions and have been selected in order to be consistent with the available studies of Pascotto et al. (2014) and Liu et al. (2009, 2010).

For the definition of wall and bulk fluid temperatures used in the computation of Bo , averaged values have been used for both cases, namely the average of the 8 thermocouples installed inside the aluminium walls for T_w , and the average between $T_{air,in}$ and $T_{air,out}$ for T_b . In view of the unavoidable measurement errors and the slightly non-uniform temperature distribution of the walls previously commented, an uncertainty of $\pm 5\%$ has to be considered for the present definition of Bo . Concerning the computation of Re_{Dh} and Ro values, the main error source comes from the measurement of the air flow rate that causes a final uncertainty of $\pm 1.5\%$.

RESULTS

2D data on plane xy'

The characterization of the separation structure downstream the ribs is obtained by the data acquired on plane xy' , i.e. a plane perpendicular to both the channel wall and the rib axis.

Figure 6 reports the reference conditions measured for the static case. The time-averaged stream tracers' path depicts a separation structure that extends up to about $x/h=3.5$ and a corner vortex located on the upstream face of the following obstacle. Contour plots of the in-plane turbulence intensity ($Tu_{xy} = ((u^2 + v^2)/2)^{0.5}/U_b$) are reported in Fig. 6(b).

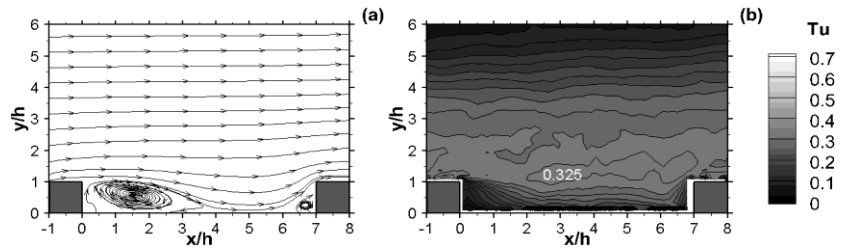


Figure 6: Stream tracers and contour plot of the in-plane turbulence intensity in plane xy' for $Ro=0$.

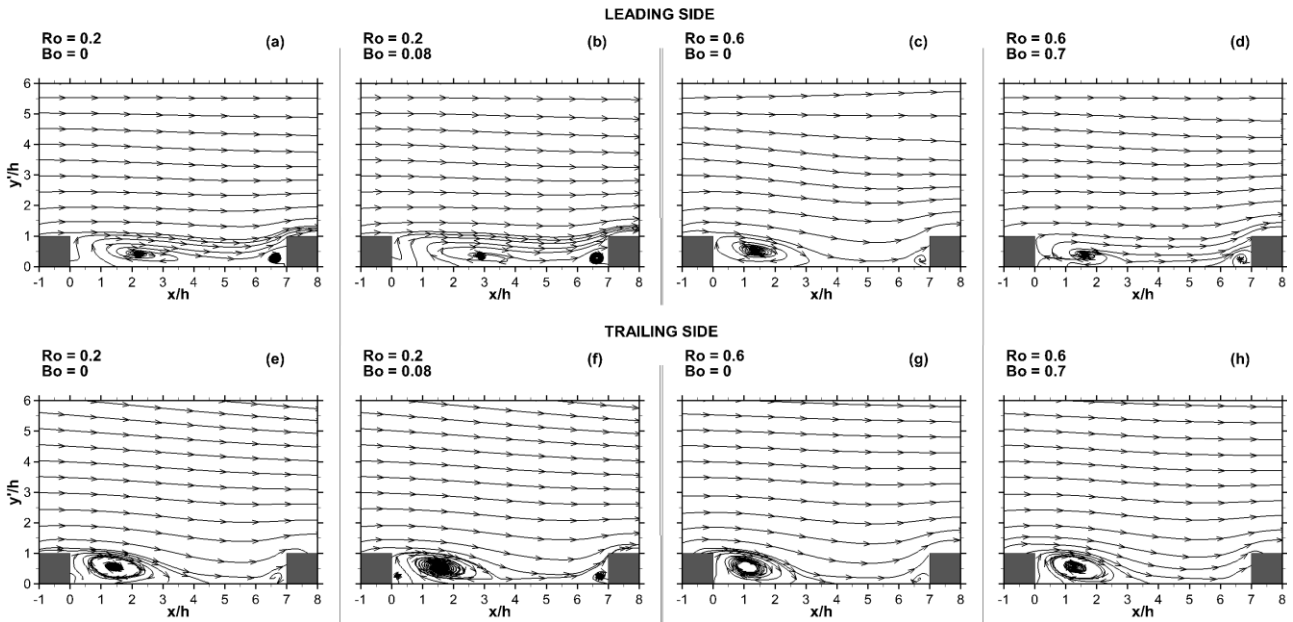


Figure 7: Stream tracers in plane xy' for all the rotating cases.

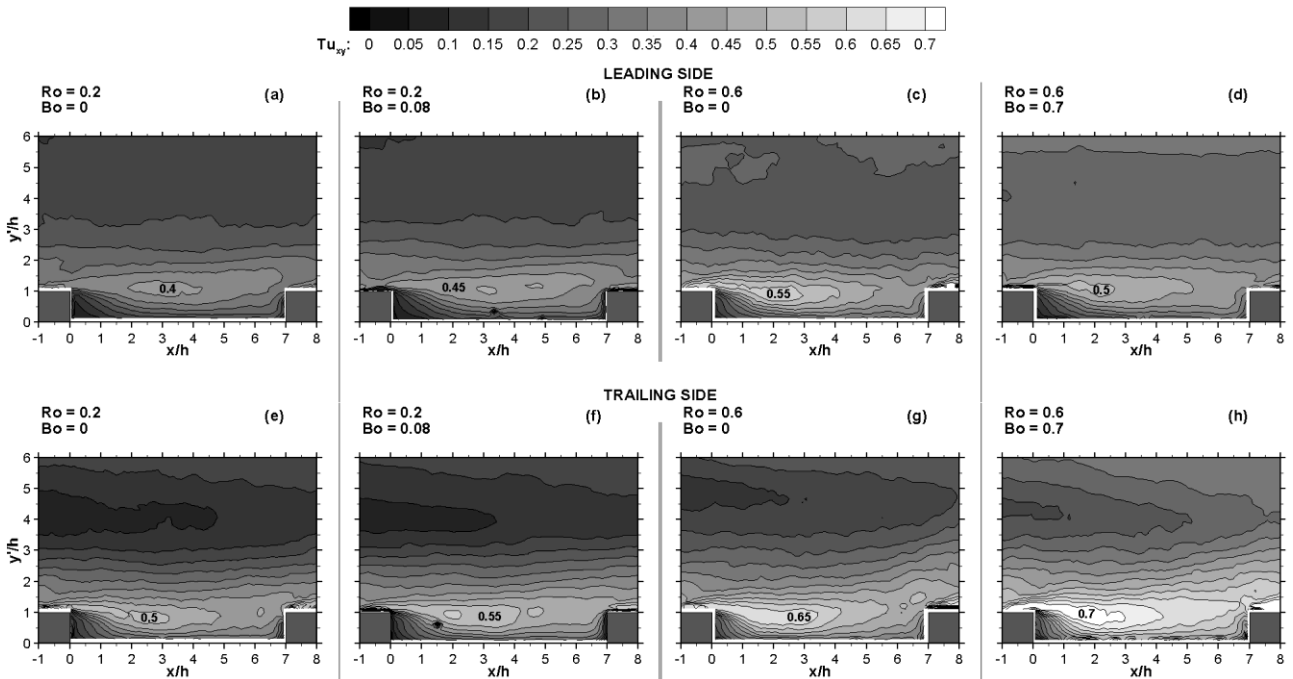


Figure 8: Contour plots of the turbulence intensity in plane xy' for all the rotating cases.

A summary of the results obtained under rotation is reported in Figs. 7 and 8 in terms of stream tracers path and Tu_{xy} levels, respectively.

When the investigated wall is at the TS (Fig. 7(e-h)), no remarkable effects of both rotation and buoyancy are observed about the flow topology, with the only exception of a small reduction of the recirculation extension found for $Ro=0.6$. Similar observations are reported also by Coletti et al. (2014) for the case of arectangular duct in orthogonal rotation. The explanation of this behaviour is linked to the destabilizing effect that rotation has on the separation structure at the TS, which causes rather strong flow turbulence that reduces the bubble extension and smoothes local density gradients. Also in the present case, higher Tu_{xy} are measured at the TS (Fig. 8(e-h)) with respect to both static case (Fig. 6(b)) and LS (Fig. 8(a-d)). More in detail, the Tu_{xy} level increases with Ro , and this effect is enhanced by buoyancy.

On the LS, the behaviour is different depending by the Ro value. At $Ro=0.2$ (Fig. 7(a, b)), the separation bubble appears longer than the static case (Fig. 6(a)), in agreement with the stabilizing effect commented by Coletti et al. (2014). Conversely, only marginal buoyancy effects are detected on both flow path and Tu_{xy} levels (Fig. 8(a, b)). This is also evident by the profiles of $\langle uv \rangle$ extracted at $y'/h=0.5$ (see Fig. 2(e)) and reported in Fig. 9(a). Indeed, the comparison of heated/non-heated cases reveals almost identical behaviours, while the destabilizing/stabilizing effects are rather clear with higher values and peaks closer to the obstacle found for TS cases. A different behaviour is found at $Ro=0.6$ (Fig. 7(c, d)), where the separation bubble gets only marginally longer with respect to the static case (Fig. 6(a)) and the flow agitation is higher for the non-heated case than the heated one (Figs. 8(c, d) and 9(b)). Nevertheless, this turned out to be only a local feature, as it will be clarified later on with the plot of Fig. 13. Finally, it is also worth to observe that the stream tracers inside the recirculation regions at the LS have a strong centripetal path that can be linked to a relevant 3D character of the flow. This evidence could be at the basis of a possible explanation of the differences commented about the present flow behaviour with respect to the one found for a rectangular channel (Coletti et al., 2014). This issue is further discussed in the next section.

3D data on plane yz

Stereo-PIV measurements in plane yz, located at 709 mm from the rotation axis (see Fig. 2(c)), have been conducted in order to characterize the rotational effects on the overall flow structure. In order to ease the present data analysis, Fig. 10 reports the results found for the smooth, non heated channel configuration obtained on the same rig by Pascotto et al. (2014). The Coriolis induced secondary flow is characterized by a vortex pair at the lowest rotation condition (see vortices A and B in Fig. 10(a)) and shows a remarkable sensitivity to the change of Ro . Indeed, at $Ro=0.4$, a third vortex (B2 in Fig. 10(b)) appears close to the LS apex, producing a rather more complex flow distribution. In Pascotto et al. (2014), a justification of this behaviour is provided and is also shown how it grows in its complexity as rotation is further increased.

The secondary flow distribution measured for the same sense of rotation of that of Fig. 10 but in the ribbed duct is reported in the plots of

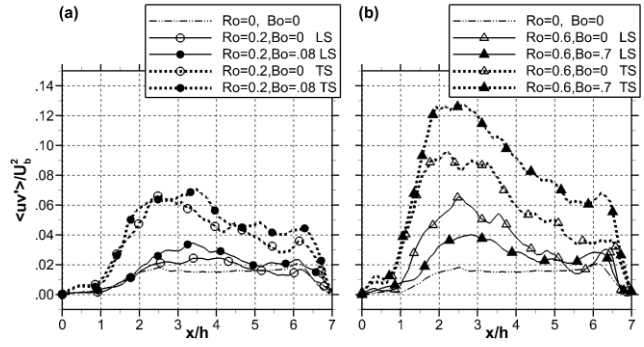


Figure 9: $\langle uv \rangle$ Reynolds stresses component extracted at $y'/h=0.5$ from plane xy'

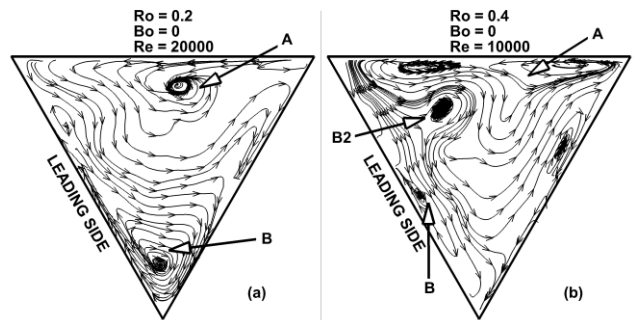


Figure 10: Stream tracers on yz for the smooth channel configuration (Pascotto et al., 2014).

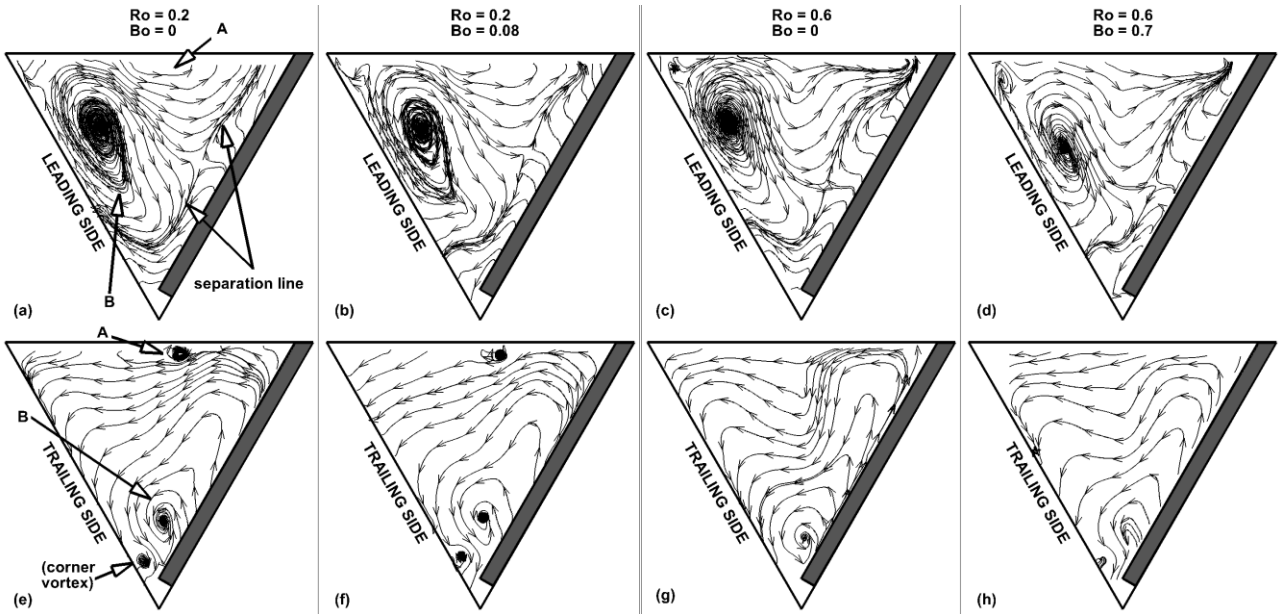


Figure 11: **Stream tracers in plane yz for all the rotating cases**

the first row of Fig. 11. With respect to the smooth case, the clockwise vortex previously found at the lower apex of the duct (vortex B in Fig. 10(a)) is now rather bigger and extends almost over all the channel cross section (B in Fig. 11(a)). The counter-clockwise vortex (A in Fig. 11(a)) is confined close to the upper, non ribbed wall and appears to be too small to be captured at the present data resolution. Moreover, the local flow acceleration on top of the rib (which region is bounded by the 3D separation line, see Fig 11(a), that extends all along the rib span at the TS) pushes the rotation induced vortices closer to the LS, causing an evident flow deviation towards the upper wall in the inter rib region at the LS. This is in agreement with the previous observation about the 3D nature of the separation found behind the obstacle (see comments about Figs.7(a-d)). Finally, if cases at different Ro are compared (see Figs. 11(a) and (c)) the sensitivity of the flow topology on plane yz to the change of Ro is practically absent, moreover also no clear effects of the buoyancy are found if heated and non heated cases are compared (see Figs. 11(b,d) and (a,c)). Slightly more evident differences can be instead appreciated in the contour plots of the U velocity component

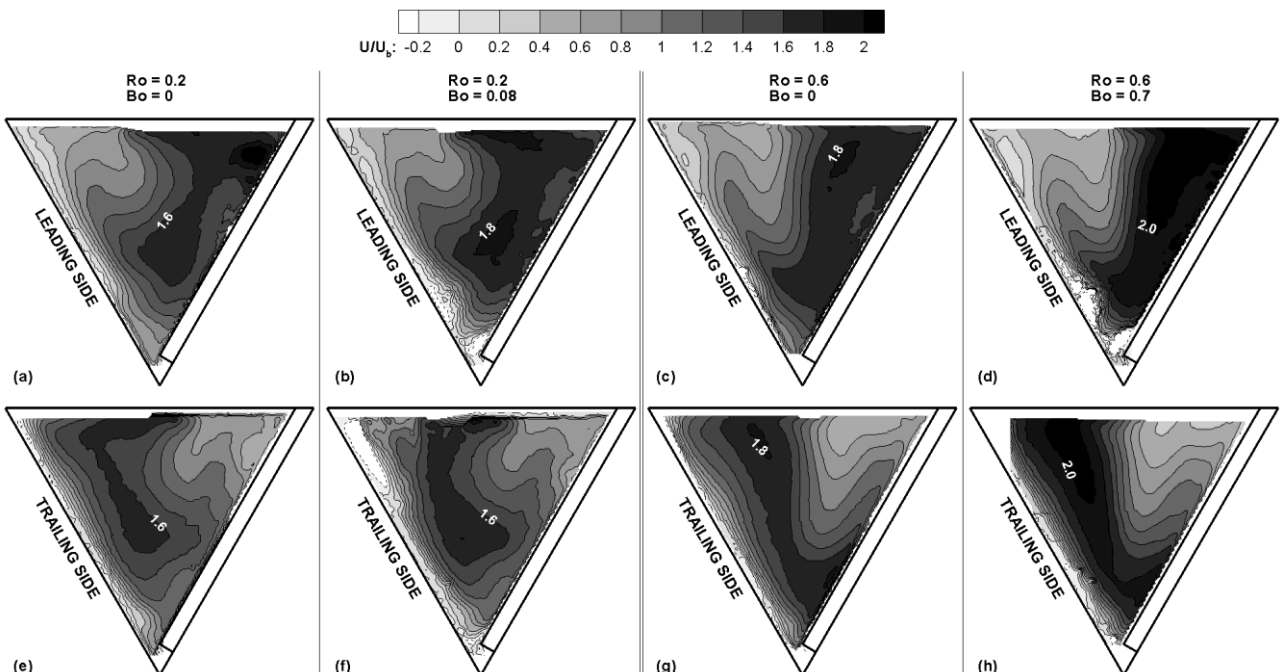


Figure 12: **Contour plots of the stream wise velocity component yz for all the rotating cases**

reported in Figs. 12(a-d). Indeed, as Ro and Bo are increased, higher velocity peaks are found at the TS as a consequence of the stronger Coriolis induced secondary structures produced at higher rotation and in view of the bigger separation bubbles found for the heated cases.

If the test section is spun in the opposite sense of rotation (Figs. 11(e-h) and 12(e-h)), the Coriolis induced vortex B is correctly found on the right of the plots and with counter-clockwise rotation, i.e. close to the LS and pushing core flow toward the TS, while vortex A is still confined close to the upper, non ribbed wall. With respect to the previous comments, the main differences concern the features of the flow in the inter-rib region at the TS that, conversely to what happens at the LS, is by far less 3D (Figs. 11(e-h)) and is characterized by a more uniform U velocity distribution (Figs. 12(e-h)). Again, slight effects caused by an increase of Ro and Bo are found only in the U velocity peaks found close to the TS (Figs. 12(e-h)).

A final comment about the effect of rotation and buoyancy can be made by looking at the Tu contour plots of Fig. 13. The stabilizing/destabilizing effect of rotation can be appreciated by comparing the Tu levels between leading and trailing sides at the same working conditions (compare frame (a) and (c) or (b) and (d)), with higher values always observed at the TS. Similarly, the stronger flow mixing promoted by buoyancy is associated to the overall higher Tu levels measured for the heated cases (compare frame (a) and (b) or (c) and (d)). This is not in contrast with the comments about Fig. 9(b). Indeed also in Fig. 13(b), at the position of plane xy' (see Fig. 2(d)) the Tu values for $Bo=0.7$ are smaller than those for non heated case in Fig. 13(a).

CONCLUSIONS

Thanks to the present study, important conclusions are drawn about the buoyancy effects on the flow field inside a ribbed triangular channel. The main findings are summarized in the following.

- Buoyancy forces have only marginal effects that result in increased velocity peaks and in an overall enhancement of the flow agitation level. No remarkable modifications are found on the rotation induced secondary flows and on the separation downstream the ribs. This behaviour differs from the results of Coletti et al. (2014) for a rectangular channel, where buoyancy lead to a dramatic increase of the separation length behind the ribs at the LS.
- On the duct cross section, rotation induced secondary flows turned out to be strongly asymmetric and characterized by a single main vortex. Consequently, the present inter-rib flow is characterized by a condition by far different from the one realized in the region of pairing of two symmetric vortices that has been investigated by Coletti et al. (2014) in a rectangular ribbed duct. It is in the authors' opinion that this evidence is at the basis of the differences here commented.

The present analysis once more confirms the complexity of the flow topology inside this kind of devices, evidence that was already discussed for the smooth case (Pascotto et al., 2014). Therefore, a precise explanation of the aero-thermal behaviour cannot be based on a simplified conjectured flow model (Liu et al., 2009) but there is the need for a deeper understanding. For this reason, the present analysis will be deepened in the near future with the help of CFD simulations over a wider range of working conditions.

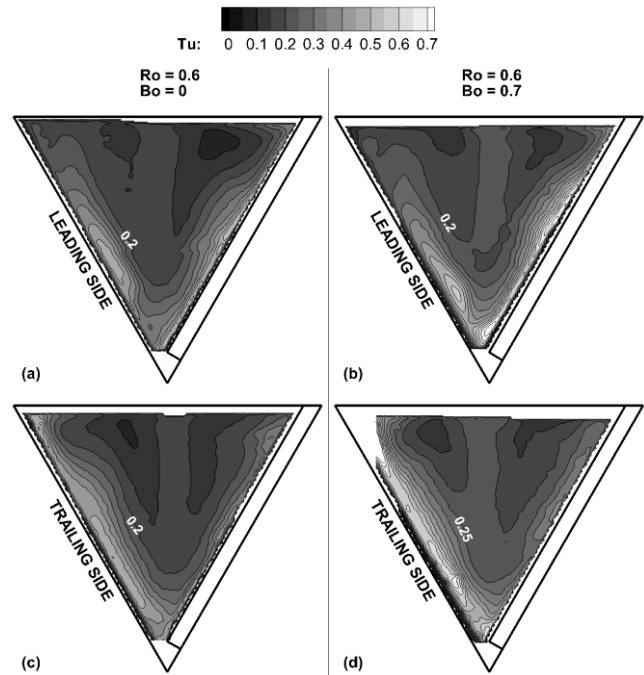


Figure 13: Tu levels in plane yz for $Ro=0.6$

ACKNOWLEDGEMENTS

This work has been supported by the Italian Ministry of University and Research (MiUR).

REFERENCES

- Armellini A., Mucignat C., Casarsa L. (2011) *Flow field analysis inside a gas turbine trailing edge cooling channel under static and rotating conditions*, Int. J. Heat Fluid Flow 32, pp. 1147–1159
- Armellini, A., Mucignat C., Casarsa L., Giannattasio P., (2012) *Flow field investigations in rotating facilities by means of stationary PIV systems*, Meas. Sci. Technol. 23, p.025302 (11pp)
- Coletti F., Maurer T., Arts T., Di Sante A., (2012) *Flow field investigation in rotating rib-roughened channel by means of particle image velocimetry*, Exp. Fluids 52, pp. 1043–1061
- Coletti F., Lo Jacono D., Cresci I., Arts T., (2014) *Turbulent flow in rib-roughened channel under the effect of Coriolis and rotational buoyancy forces*, Physics of Fluids 26, p. 045111
- Elfert, M., Schroll, M., Förster, W. (2012) *PIV measurement of secondary flow in a rotating two-pass cooling system with an improved sequencer technique*, Journal of Turbomachinery, 134 (3), art. no. 031001
- Johnston J. P., Halleen R. P., Lezius D. K. (1972) *Effects of spanwise rotation on the structure of two-dimensional fully developed turbulent channel flow* J. Fluid Mech. 56, pp. 533–557
- Lei, J., Li, S.-J., Han, J.-C., Zhang, L., Moon, H.-K. (2014) *Effect of a turning vane on heat transfer in rotating multipass rectangular smooth channel*, Journal of Thermophysics and Heat Transfer, 28 (3), pp. 417-427
- Liu Y.H., Huh M., Rhee D.H., Han J.C., Moon H.K.K. (2009) *Heat Transfer in Leading Edge, Triangular Shaped Cooling Channels With Angled Ribs Under High Rotation Numbers*, ASME J. Turbomach., 131(4), p. 041017
- Liu Y.H., Huh M., Han J.C., Moon, H.K. (2010) *High Rotation Number Effect on Heat Transfer in a Triangular Channel With 45 deg, Inverted 45 deg, and 90 deg Ribs*, ASME J. Heat Trans., 132(7), p. 071702
- Morris W. D., Ayhan T. (1979) *Observation on the influence of rotation on heat transfer in the coolant channel of gas turbine rotor blade*, Proc. Inst. Mech. Engrs. 193, pp. 303–311
- Mucignat C., Armellini A., Casarsa L., (2013) *Flow field analysis inside a gas turbine trailing edge cooling channel under static and rotating conditions: Effect of ribs*, Int. J. Heat Fluid Flow 42, pp. 236–250
- Pascotto M., Armellini A., Mucignat C., Casarsa L. (2014) *Coriolis Effects on the Flow Field Inside a Rotating Triangular Channel for Leading Edge Cooling*, ASME J. Turbomach., 136(3), p.031019
- Speziale, C. G., Thangam S. (1983) *Numerical Study of Secondary Flows and Roll-Cell Instabilities in Rotating Channel Flow*, J. Fluid. Mech., 130, pp. 377–395.
- Willert, C. (1997), *Stereoscopic Digital Particle Image Velocimetry for Application in Wind Tunnel Flows*,” Meas. Sci. and Technol., 8, pp. 1465–1497